VERSITA

Acta Geophysica
vol. 60, no. 5, Oct. 2012, pp. 1474-1492
DOI: 10.2478/s11600-012-0063-3

Direct Evaluation of Refractive-Index Structure Functions from Large-Eddy Simulation Output for Atmospheric Convective Boundary Layers

Christopher WILSON and Evgeni FEDOROVICH

School of Meteorology, University of Oklahoma, Norman, OK, USA
e-mails: chris.wilson@ou.edu, fedorovich@ou.edu (corresponding author)

Abstract

Fluctuations of the refractive index associated with atmospheric turbulence affect the propagation of electromagnetic and acoustic waves in the atmosphere. In the reported study, the effects of turbulence on wave propagation in the atmospheric convective boundary layer (CBL) are considered in terms of the second-order refractive index structure function and related to its structure-function parameter C_n^2. Two structure-function evaluation methods are compared. The direct evaluation method involves calculating the refractive index at each point in the simulation domain with subsequent calculation of the structure function. The second method is based on a parameterized linear relationship between the refractive-index structure function and temperature/humidity structure functions. For each evaluation method, vertical profiles of C_n^2 computed for separations along the three coordinate directions collapse together over a significant portion of the CBL. Near-surface divergence of C_n^2 values along the horizontal directions was noted and attributed to the influence of surface wind shear on the turbulent fluctuations of temperature and humidity. The behavior of C_n^2 near the surface was shown to agree favorably with similarity-theory predictions.

Key words: turbulence, boundary layer, refractive index, structure function, numerical simulation.

1. INTRODUCTION

Fluctuations of the refractive index associated with atmospheric turbulence can strongly affect the propagation of electromagnetic and acoustic waves in the atmosphere. The scattering of electromagnetic radiation and sound waves caused by such fluctuations can have a significant influence on many applications. For instance, images viewed through a telescope suffer reduced resolution as a result of this scattering (Burk 1980). The performance of communication systems is impacted by refractive-index fluctuations (Cheinet and Siebesma 2009). The returns measured by remote sensing instruments used to investigate atmospheric flow structure, such as radars and sodars, also depend on spatial variability of the refractive index.

The effects of atmospheric turbulence on wave propagation are typically considered (Tatarskii 1961) in terms of the second-order refractive index structure function given by

$$\overline{(\delta n)^2}\,(\mathbf{r},t) = \overline{\left[n(\mathbf{x},t) - n(\mathbf{x}+\mathbf{r},t)\right]^2}\ , \tag{1}$$

where the overbar represents ensemble averaging, n is the refractive index, $\mathbf{r}$ is the separation vector, $\mathbf{x}$ is the position vector, and t is time. For separations $r = |\mathbf{r}|$ within the inertial subrange of spatial scales of n's turbulent fluctuations, the refractive-index structure function has the form (Tatarskii 1961, Wyngaard 2010):

$$\overline{(\delta n)^2} = C_n^2\, r^{2/3}\ , \tag{2}$$

where C_n^2 is the so-called refractive-index structure-function parameter.

In the planetary boundary layer, pressure fluctuations may have some influence on refractive-index fluctuations, but are generally considered to be of negligible importance (Burk 1980, McBean and Elliott 1981, Andreas 1988). The fluctuation of n in space, δn, is found to be primarily associated with corresponding fluctuations $\delta\theta$ and δq of potential temperature θ and specific humidity q, respectively (Peltier and Wyngaard 1995). Following Andreas (1988) and Peltier and Wyngaard (1995), one can assume a linear form for this relationship and write

$$\delta n = A\delta\theta + B\delta q\ , \tag{3}$$

where A and B are coefficients that depend on temperature, humidity, pressure, and the type of wave being considered. The second-order refractive index structure function is then given by

$$\overline{(\delta n)^2} = A^2\overline{(\delta\theta)^2} + 2AB\overline{(\delta\theta\delta q)} + B^2\overline{(\delta q)^2}\ , \tag{4}$$

where $\overline{(\delta\theta)^2}$, $\overline{(\delta q)^2}$, and $\overline{(\delta\theta\delta q)}$ are the potential temperature, specific humidity, and joint temperature-humidity structure functions, respectively, given by

$$\overline{(\delta\theta)^2}(\mathbf{r},t) = \overline{[\theta(\mathbf{x},t)-\theta(\mathbf{x}+\mathbf{r},t)]^2} \ , \tag{5}$$

$$\overline{(\delta q)^2}(\mathbf{r},t) = \overline{[q(\mathbf{x},t)-q(\mathbf{x}+\mathbf{r},t)]^2} \ , \tag{6}$$

$$\overline{(\delta\theta\delta q)}(\mathbf{r},t) = \overline{[\theta(\mathbf{x},t)-\theta(\mathbf{x}+\mathbf{r},t)][q(\mathbf{x},t)-q(\mathbf{x}+\mathbf{r},t)]} \ . \tag{7}$$

For separations r within the inertial subrange, structure-function parameters for temperature and humidity are defined similarly to C_n^2 as

$$\overline{(\delta\theta)^2} = C_T^2 \, r^{2/3} \ , \tag{8}$$

$$\overline{(\delta q)^2} = C_q^2 \, r^{2/3} \ , \tag{9}$$

$$\overline{(\delta\theta\delta q)} = C_{Tq} \, r^{2/3} \ . \tag{10}$$

Making use of Eq. (2) and being substituted in Eq. (4), the above expressions may be employed, as shown in Wyngaard *et al*. (1978), to relate the refractive-index structure-function parameter C_n^2 to the structure-function parameters of temperature and humidity (C_T^2, C_q^2, and C_{Tq}) in the following way:

$$C_n^2 = A^2 C_T^2 + 2ABC_{Tq} + B^2 C_q^2 \ . \tag{11}$$

Structure-function parameters C_T^2, C_q^2, and C_n^2 may in turn be related to one-dimensional inertial-subrange spectra of the corresponding quantities. Following Tatarskii (1961), Essenwanger and Reiter (1969) and Wyngaard *et al*. (1971), and using the temperature field as an example, the one-dimensional spectrum of temperature fluctuations in the inertial subrange may be expressed through the temperature structure-function parameter as

$$\Phi_T(k) = 0.25 \, C_T^2 k^{-5/3} \ , \tag{12}$$

where k is the wavenumber.

On the other hand, Obukhov (1949) and Corrsin (1951) showed that temperature spectrum in the inertial subrange can also be expressed as

$$\Phi_T(k) = \beta\chi_T \, \epsilon^{-1/3} \, k^{-5/3} \ , \tag{13}$$

where χ_T is the molecular destruction rate of half temperature variance, ϵ is the dissipation rate of turbulence kinetic energy (TKE), and β is a universal dimensionless constant. Taking $\beta = 0.8$ as suggested by Wyngaard and Cotè (1971), and combining Eqs. (12) and (13), one comes to

$$C_T^2 = 3.2\chi_T \epsilon^{-1/3} \quad . \tag{14}$$

The one-dimensional refractive-index spectrum, the one-dimensional humidity spectrum, and the temperature-humidity co-spectrum (Wyngaard and LeMone 1980, Andreas 1988) may be expressed, respectively, in the form analogous to Eq. (12):

$$\Phi_n(k) = 0.25 C_n^2 k^{-5/3} \quad , \tag{15}$$

$$\Phi_q(k) = 0.25 C_q^2 k^{-5/3} \quad , \tag{16}$$

$$\Phi_{Tq}(k) = 0.25 C_{Tq} k^{-5/3} \quad . \tag{17}$$

Consequently,

$$C_n^2 = 3.2\chi_n \epsilon^{-1/3} \quad , \tag{18}$$

$$C_q^2 = 3.2\chi_q \epsilon^{-1/3} \quad , \tag{19}$$

$$C_{Tq} = 3.2\chi_{Tq} \epsilon^{-1/3} \quad , \tag{20}$$

where χ_n, χ_q, and χ_{Tq} are the molecular destruction rates of half refractive index variance, half humidity variance, and half temperature-humidity covariance, respectively.

The parameterized relationships (18)-(20) have been previously used to determine structure-function parameters in observational studies (see *e.g.*, Wyngaard *et al*. 1971, Kaimal *et al*. 1976, Kohsiek 1988) and using numerical large-eddy simulation (LES) outputs (Peltier and Wyngaard 1995, Cheinet and Siebesma 2009, Cheinet and Cumin 2011). On the other hand, some investigators have also employed expressions like Eqs. (1), (2) and (5)-(10) to directly calculate structure functions and structure-function parameters from measurement data (see *e.g.*, van den Kroonenberg *et al*. 2012).

In the present study, numerical LES output is used to directly evaluate $\overline{(\delta n)^2}$ in the turbulent atmospheric convective boundary layer (CBL) and investigate behavior of C_n^2 in the inertial subrange. For comparison, C_n^2 is also evaluated using approximate formula (11) relating C_n^2 to the structure-function parameters C_T^2, C_q^2, and C_{Tq} which are directly calculated from temperature and humidity fields generated by LES.

2. EXPERIMENTAL DESIGN

2.1 Large-eddy simulation

Large-eddy simulation is used in this study to generate realistic temporally and spatially variable three-dimensional CBL potential temperature and specific humidity fields (in addition to flow velocity fields). It appears attractive to use LES output to directly evaluate structure functions in the turbulent CBL given the availability of flow variables at every point in the simulation domain at every time step. The employed LES code, which features a subgrid TKE closure following Deardorff (1980), has been shown to confidently reproduce turbulence structure in the CBL (Fedorovich *et al*. 2004a, b).

Results from two simulation runs will be considered in this study. Both simulation setups employed a numerical grid spacing of 10 m and a domain size of $(X \times Y \times Z) = 2.56 \times 2.56 \times 3$ km^3. These horizontal dimensions were proven, through previous numerical experiments, to be sufficient for reproduction of turbulence statistics within our target scale ranges (up to several hundreds of meters) in a moderately sheared CBL.

The first simulation, denoted as LES10, is a simulation of realistic planetary boundary layer evolution that was observed at the Lamont, Oklahoma, Atmospheric Radiation Measurement (ARM) Program site on 31 May 2009. A wide array of meteorological instrumentation is located at the ARM site, making it an appealing location for positioning numerical simulation domains. Surface sensible and latent heat fluxes that provided the surface forcing for the LES10 simulation were prescribed using data from the ARM eddy correlation flux measurement system (ECOR; Cook and Pekour 2008), and the geostrophic wind profiles (representing the pressure-gradient forcing) were retrieved from the Rapid Update Cycle (RUC; Benjamin *et al*. 1994) model. ECOR fluxes are available as 30-minute averages, and RUC profiles are available hourly.

A force-restore method was used to nudge the horizontally averaged LES10 solutions of potential temperature θ, specific humidity q, and horizontal (along the x and y directions) flow velocity components u and v toward the corresponding profiles available from the RUC model (see Gibbs *et al*. 2011). This nudging procedure is designed to account for atmospheric variability on scales larger than the scale of the LES domain. At each LES time step, a force-restore term $\mathcal{F}_{\tilde{\phi}}(z)$ was determined using

$$\mathcal{F}_{\tilde{\phi}}(z) = \frac{\phi(z)_{\mathrm{RUC}} - \overline{\tilde{\phi}}(z)_{\mathrm{LES}}}{t_r}\,, \tag{21}$$

where $\tilde{\phi}$ is the filtered (in the LES sense) variable of interest (θ, q, u, or v), $\phi(z)_{\mathrm{RUC}}$ is the temporally interpolated RUC profile of the variable of interest,

t_r is a nudging time constant, and $\overline{\tilde{\phi}}(z)_{\mathrm{LES}}$ is the horizontal plane average of the LES variable of interest at the preceding time step. The force-restore term was added to the right-hand side of prognostic equation for the corresponding variable at each time step. In the conducted study, t_r was taken equal to 3600 s. This provided an adjustment time scale that was larger than the typical CBL overturn time scale (which is of the order of a fraction of an hour), but smaller than the time scale of the boundary layer diurnal variation. With such prescribed value of the force-restore time constant, the implemented nudging did not noticeably affect turbulent fluctuations within the scale ranges of interest for this study (with time scales up to ten minutes and length scales up to several hundred meters).

The second simulation run, denoted as LES10EMF, was performed with enhanced surface moisture flux. The other setup parameters were the same as in the LES10 run. The RUC model data and the nudging procedure were also implemented in the manner analogous to the LES10 run. The surface sensible heat flux remained the same as in LES10 (with the heat-flux data taken from the ARM ECOR instrument), while the surface latent heat flux was prescribed as five times larger than in LES10.

2.2 Structure function evaluation

The LES provides simultaneous fields of potential temperature θ and specific humidity q at each time step and in every grid cell of the simulation domain. As such, $\overline{(\delta n)^2}$, $\overline{(\delta\theta)^2}$, $\overline{(\delta q)^2}$, and $\overline{(\delta\theta\delta q)}$ can be evaluated from the LES output directly by using Eqs. (1) and (5)-(7), *i.e.*, without invoking supplementary relationships involving dissipation and destruction rates.

In order to evaluate $\overline{(\delta n)^2}$ at given time step, the refractive index n is first calculated in each grid point of the simulation domain. For wavelengths within the visible-radiation range, n may be determined following Andreas (1988) and Frederickson *et al*. (2000) as

$$n = 1 + 10^{-6}\left\{m_1(\lambda)\frac{p}{T} + \left[m_2(\lambda) - m_1(\lambda)\right]\frac{qP}{T\varepsilon_q\gamma}\right\}, \tag{22}$$

where λ [μm] is the wavelength of interest, P [hPa] is atmospheric pressure, T [K] is absolute temperature, $\varepsilon_q = 0.62197$, q [gg^{-1}] is specific humidity, and $\gamma = (1 + 0.61\,q)$. Parameters m_1 and m_2 are given by

$$m_1(\lambda) = 23.7134 + \frac{6839.397}{130 - \lambda^{-2}} + \frac{45.473}{38.9 - \lambda^{-2}}, \tag{23}$$

$$m_2(\lambda) = 64.8731 + 0.58058\lambda^{-2} - 0.0071150\lambda^{-4} + 0.0008851\lambda^{-6} \ . \qquad (24)$$

In our study, squared differences of n were calculated in space as functions of separation distance. These calculations were carried out using separations in the x and y directions horizontally, and in the z direction vertically. The separations used were integer multiples of the LES grid spacing Δ which is uniform in all directions.

Evaluation of the second-order refractive index structure function in the x direction was conducted for each time t and height index z in the LES output by calculating

$$(\delta n)^2\Big|_x (t, z, x_i, y, x) = \left[n(t, z, y, x) - n(t, z, y, x + x_i) \right]^2 \qquad (25)$$

at an individual point (represented by x and y index pair) in the horizontal plane and adding it to a running sum of such values corresponding to the current value of x_i. Here, x_i determines the separation distance to which spatial differences correspond. Initially $x_i = \Delta$, and the $(\delta n)^2\Big|_x$ values were calculated between neighboring grid points. The running sum was only modified if $x + x_i \le X$, where X is the domain size in the x direction.

When all possible calculations had been performed in the horizontal plane at the current height and time, the running sum was averaged. The value of x_i was then increased (from Δ to 2Δ), the running sum was reset, and the calculation process was repeated. This calculation procedure was carried out for incrementally larger integer values of x_i until the maximum desired separation distance was reached or until squared differences can no longer be calculated. Of course, the number of incremental sums contributing to the horizontal plane averages would be smaller for larger separations. After squared differences were calculated for the largest separation, the entire procedure was repeated for the next height z.

Once these calculations had been performed for all separations, heights, and times, the horizontal plane averages were additionally averaged in time. This provided the following direct estimate for the refractive-index structure function in x direction:

$$\overline{(\delta n)^2}\Big|_x (z, i\Delta) = \left\langle (\delta n)^2\Big|_x (t, z, x_i, y, x) \right\rangle_{x,y,t} \ , \qquad (26)$$

where $i\Delta = x_i$ is the separation distance in the x direction and the angle brackets signify the aforementioned averaging over horizontal planes supplemented by averaging in time which in the reported study was performed over a one-hour time period (see the ending statement of this section). The number of flow realizations in time was corresponding to the number of LES

time steps within the averaging time period (about 3600 with the time step being in average 1 s).

The same calculation procedure was applied to obtain the direct estimate of the refractive-index structure function in the y direction with the squared difference computed as

$$(\delta n)^2\Big|_y (t,z,y_j,y,x) = \left[n(t,z,y,x) - n(t,z,y+y_j,x)\right]^2 , \tag{27}$$

where y_j is the separation distance in the y direction, and the structure function evaluated as

$$\overline{(\delta n)^2}\Big|_y (z,j\Delta) = \left\langle (\delta n)^2\Big|_y (t,z,y_j,y,x)\right\rangle_{x,y,t} , \tag{28}$$

where $j\Delta = y_j$ is the separation distance in the y direction. The largest separation distance used in the structure-function calculations in x and y directions was 1000 m.

Evaluation of the refractive-index structure function in the vertical direction slightly differed from the procedures used for evaluation of the functions in x and y directions. In this case, fluctuations of n from horizontal plane averages were first calculated in order to exclude the influence of the mean vertical gradient of n in structure function calculations. The resulting squared difference (denoted with the *zp* subscript) appeared as

$$(\delta n)^2\Big|_{zp} (t,z,z_k,y,x) = \frac{1}{2}\left(\left[n'(t,z,y,x) - n'(t,z+z_k,y,x)\right]^2 + \left[n'(t,z,y,x) - n'(t,z-z_k,y,x)\right]^2\right) , \tag{29}$$

where z_k is the separation distance in the z direction at each x, y point and n' is the fluctuation of n from its horizontal plane average value. In this way, $(\delta n)^2\Big|_{zp}$ was calculated as the average of squared differences in the positive and negative vertical directions. The ability to do calculations was therefore limited by the actual value of z_k and by the proximity of the height of interest to the lower or upper limits of the LES domain. The combined averaging procedure analogous to the one outlined for structure function evaluation in the x and y directions was then used, resulting in

$$\overline{(\delta n)^2}\Big|_{zp} (z,k\Delta) = \left\langle (\delta n)^2\Big|_{zp} (t,z,z_k,y,x)\right\rangle_{x,y,t} , \tag{30}$$

the directly evaluated refractive-index structure function in the z direction for the separation distance $k\Delta = z_k$. Largest possible separation distance for

$\overline{(\delta n)^2}\Big|_{zp}$ at given elevation z was thus determined by this elevation and by the distance from the domain top.

The same methods were used to directly calculate $\overline{(\delta\theta)^2}$, $\overline{(\delta q)^2}$, and $\overline{(\delta\theta\delta q)}$ in x, y, and z directions from the LES potential temperature and humidity fields. In order to estimate C_n^2 from Eq. (11), structure-function parameters C_T^2, C_q^2, and C_{Tq} were determined using Eqs. (8) to (10) from the corresponding structure-function dependencies in the inertial subranges. The coefficients A and B were prescribed following Andreas (1988).

All structure function and structure-function parameter values discussed in the following sections were evaluated from simulation runs LES10 and LES10EMF for the hour-long period 19:00 through 20:00 UTC on 31 May 2009.

3. RESULTS

3.1 Flow statistics in simulated CBLs

The main features of CBL structure from simulations LES10 and LES10EMF are illustrated in Fig. 1 with solid and dashed lines, respectively. Profiles of potential temperature θ, specific humidity q, flow velocity components u and v, potential temperature variance $\overline{\theta'\theta'}$, specific humidity variance $\overline{q'q'}$, potential temperature-specific humidity co-variance $\overline{\theta'q'}$, and virtual potential temperature flux $\overline{w'\theta_v'}$, where w is the vertical component of the flow velocity and the primes signify deviations from the plane means, are included. All shown statistics have been obtained by the plane averaging, and then additionally averaged in time between 19:00 and 20:00 UTC on 31 May 2009. This hour-long period corresponds to the time frame over which the structure function data have also been obtained (see Section 2.2).

The vertical profile of θ from simulation LES10 in Fig. 1 shows a relatively well-mixed CBL interior where changes of θ with height are rather minor. In the lower CBL portion, potential temperature increases toward the warm surface as a result of the heat transfer. The capping inversion marked by a notable potential temperature increase at the height of about 1.5 km is also clearly seen. The vertical profile of q from simulation LES10 mirrors features seen in the θ profile except for the near-surface region.

Profiles of the horizontal velocity components show that momentum is also relatively well mixed in the CBL interior, and that the mean flow is south-southwesterly throughout the depth of the CBL. The $\overline{\theta'\theta'}$ profile shows

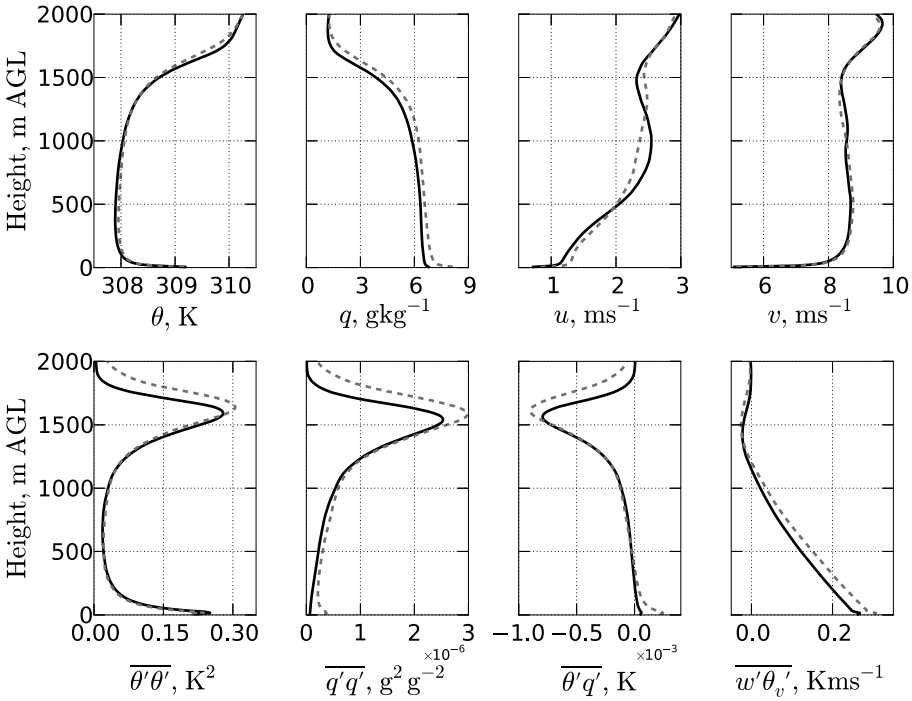

Fig. 1. Vertical profiles of potential temperature θ, specific humidity q, horizontal flow velocity components u and v, potential temperature variance $\overline{\theta'\theta'}$, specific humidity variance $\overline{q'q'}$, potential temperature-specific humidity covariance $\overline{\theta'q'}$, and virtual potential temperature flux $\overline{w'\theta_v'}$ from simulations LES10 (solid lines) and LES10EMF (dashed lines).

near-surface and entrainment zone maxima, while the $\overline{q'q'}$ profile has a distinct maximum only in the entrainment zone. Values of $\overline{q'q'}$ in the lower portion of the CBL are relatively small as a result of the weak surface latent heat flux both measured by the ARM ECOR system and prescribed in simulation LES10. The structure of the $\overline{\theta'q'}$ and $\overline{w'\theta_v'}$ profiles in Fig. 1 is generally consistent with the structure observed in the CBL (see *e.g.*, Wyngaard *et al*. 1978).

Shapes of the θ and q profiles from simulation LES10EMF in Fig. 1 are overall rather similar to those from simulation LES10. The specific humidity is increased slightly in simulation LES10EMF as a result of the enhanced latent heat flux, but the nudging procedure keeps the mean values of q from increasing greatly. The velocity-component and $\overline{\theta'\theta'}$ profiles also remain

quite similar. However, the specific humidity variance $\overline{q'q'}$ is noticeably larger in LES10EMF both in the entrainment zone and near the surface. The enhanced latent heat flux also results in anticipated increases of $\overline{w'\theta_v'}$ and near-surface temperature-humidity covariance in LES10EMF.

3.2 Structure functions

Refractive index structure functions evaluated using the two methods described in Section 2.2 are functions of height and the separation distance $r = (x_i, y_j, z_k)$. Plotting structure function values *versus* separation distance reveals the extent to which structure functions evaluated in the x, y, and z directions relate to each other. In addition, such a plot shows the range of separations for which the structure functions exhibit a $r^{2/3}$ dependence expected for the inertial subrange. Only for separations within the inertial subrange does the refractive index structure-function parameter defined as in Eq. (2) make sense.

Figure 2 shows the refractive index structure functions $\overline{(\delta n)^2}\Big|_x$, $\overline{(\delta n)^2}\Big|_y$, and $\overline{(\delta n)^2}\Big|_{zp}$ evaluated directly in all three directions at a height of 745 m (that is, within the mixed region of the CBL) from the LES10EMF simulation. The refractive index values correspond to an electromagnetic radiation wavelength of 0.55 μm following Andreas (1988). For separations from approximately 40 through 200 m, values of structure functions along individual directions collapse together and all tend to exhibit a $r^{2/3}$ behavior.

For separations larger than 200 m, structure functions for different directions begin to diverge. Values of $\overline{(\delta n)^2}\Big|_{zp}$ increase relatively rapidly with increasing separation distance because larger separations correspond to differences in the refractive index between portions of the CBL with essentially different characteristics. Thus, even with the removal of horizontal plane averages prior to structure function evaluation, values of $\overline{(\delta n)^2}\Big|_{zp}$ become large as squared differences are being calculated between points in the mixed layer and the entrainment zone (or free atmosphere above it), or between points in the mixed layer and in the surface layer. The drop off in the magnitudes of the structure function values for separations smaller than approximately 40 m is attributable to the combined effect of the finite differencing and damping by the LES subfilter-scale model. This decline in structure function values represents a reduction in the spatial variability in the refractive-index field at smaller separations (higher wavenumbers).

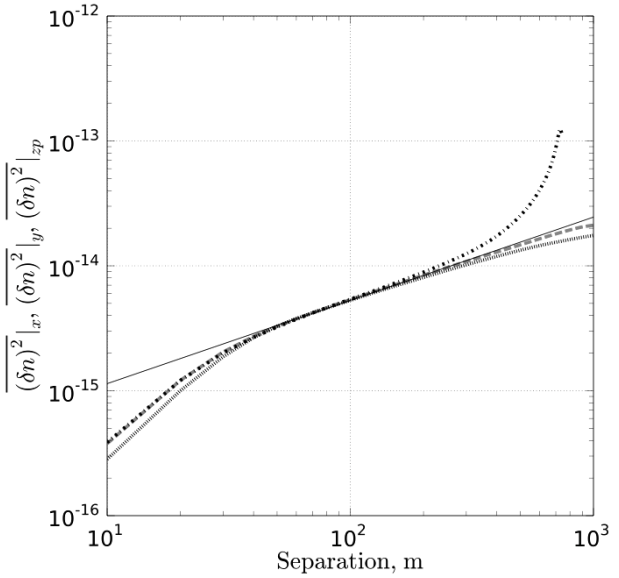

Fig. 2. Directly evaluated second-order refractive index structure functions $\overline{(\delta n)^2}\Big|_x$ (dashed line), $\overline{(\delta n)^2}\Big|_y$ (dotted line), and $\overline{(\delta n)^2}\Big|_{zp}$ (dashed-dotted line) *versus* separation distance from simulation LES10EMF at height 745 m. Refractive index calculations correspond to a wavelength of 0.55 μm. The straight black reference line represents the $r^{2/3}$ dependence.

In addition to the results from simulations LES10 and LES10EMF, a similar analysis conducted with output from simulations using coarser and finer grid spacings (not included here) indicated that the smallest separation at which values of $\overline{(\delta n)^2}$ begin to exhibit a $r^{2/3}$ dependence appears to be approximately 4Δ. This extension of 2/3-law behavior to smaller separations with decreasing simulation grid spacing is quite expectable as more scales in the flow are explicitly resolved and the effects of the subfilter-scale model become less important.

Values of $\overline{(\delta n)^2}\Big|_x$, $\overline{(\delta n)^2}\Big|_y$, and $\overline{(\delta n)^2}\Big|_{zp}$ estimated using Eq. (4) and plotted *versus* separation distance (not shown) exhibit very similar behavior to that observed in Fig. 2 for the directly evaluated structure functions. As such, refractive-index structure functions obtained by both methods outlined in Section 2.2 can be used to compute refractive-index structure-function parameters through Eq. (2) for separations for which the directly evaluated structure functions exhibit 2/3-law behavior (see Fig. 2).

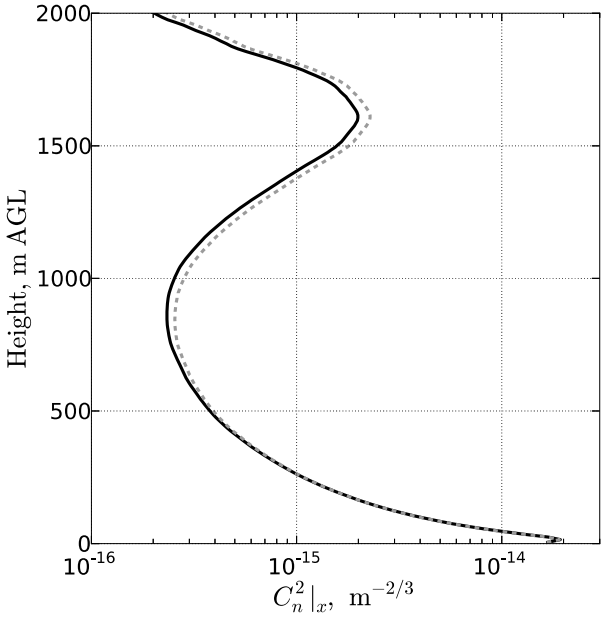

Fig. 3. Vertical profiles of $C_n^2\big|_x$ calculated from the simulation LES10EMF using the two methods outlined in Section 2.2. Directly evaluated $C_n^2\big|_x$ (solid line) and $C_n^2\big|_x$ estimated from C_T^2, C_q^2, and C_{Tq} using Eq. 11 (dashed line) correspond to a wavelength of 0.55 μm.

Figure 3 shows vertical profiles of $C_n^2\big|_x$ from simulation LES10EMF evaluated directly and estimated from C_T^2, C_q^2, and C_{Tq} using Eq. (4) for a wavelength of 0.55 μm. Profiles of $C_n^2\big|_y$ and $C_n^2\big|_{zp}$ are quite similar and are not presented. Structure-function parameters in Fig. 3 indicate that in the lower portion of the CBL both methods for determining $C_n^2\big|_x$ provide very close results. In the upper portion of the CBL, however, differences become noticeable. Conceivably, these differences (which are rather minor overall) result from effects omitted in the adopted linear relationship (4) between the refractive index on one side, and potential temperature and specific humidity on the other side. Above approximately 500 m, values of $C_n^2\big|_x$ estimated using C_T^2, C_q^2, and C_{Tq} tend to be larger than values of $C_n^2\big|_x$ evaluated directly from the refractive-parameter structure function.

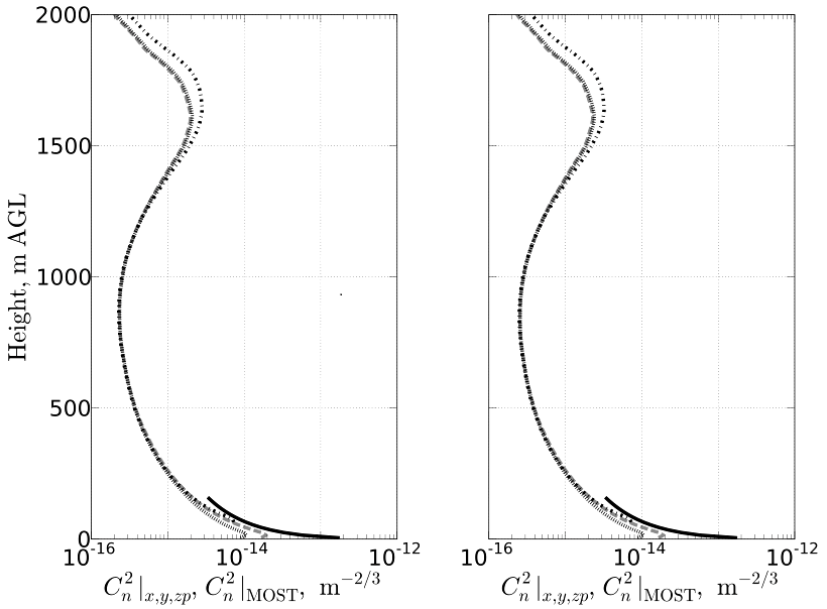

Fig. 4. Vertical profiles of $C_n^2\big|_x$ (dashed line), $C_n^2\big|_y$ (dotted line), and $C_n^2\big|_{zp}$ (dashed-dotted line) from simulation LES10EMF evaluated directly (left) and estimated through C_T^2, C_q^2, and C_{Tq} (right). Structure-function parameters correspond to a separation distance of 60 m and have been calculated for a wavelength of 0.55 μm. The solid black curves (identical in both panels) represent the MOST C_n^2 prediction following Andreas (1988).

It appears instructive to further evaluate the agreement between directly evaluated $C_n^2\big|_x$, $C_n^2\big|_y$, and $C_n^2\big|_{zp}$ and their counterparts estimated from temperature and humidity structure-function parameters. The left panel in Fig. 4 shows vertical profiles of the directly evaluated refractive index structure-function parameters from simulation LES10EMF. The solid black curve represents the Monin–Obukhov similarity theory (MOST) surface-layer C_n^2 prediction following Andreas (1988). Near the surface, the behavior of directly evaluated $C_n^2\big|_x$, $C_n^2\big|_y$, and $C_n^2\big|_{zp}$ with height tends to agree relatively well with the similarity theory prediction. The inability of the LES to fully resolve the variability in the temperature field near the surface is an apparent reason for the smaller values of the directly evaluated structure-function parameters relative to the MOST prediction very close to the sur-

face. The divergence of $C_n^2\big|_x$ and $C_n^2\big|_y$ near the surface is apparently associated with the flow anisotropy resulting from surface wind shear.

Marked similarity of $C_n^2\big|_x$, $C_n^2\big|_y$, and $C_n^2\big|_{zp}$ at a height of 745 m has already been pointed out in Fig. 2. Figure 4 shows that this similarity extends vertically through a significant portion of the CBL. The larger values of $C_n^2\big|_{zp}$ in the upper portion of the CBL result from the differences calculated in the vertical direction between sublayers with considerably different refractive parameter values. The right panel in Fig. 4 shows vertical profiles of $C_n^2\big|_x$, $C_n^2\big|_y$, and $C_n^2\big|_{zp}$ estimated using C_T^2, C_q^2, and C_{Tq} from simulation LES10EMF. The shapes of these profiles are nearly indistinguishable from those of the directly evaluated structure-function parameters in the left panel of Fig. 4. Consequently, the analysis provided above applies to profiles in the right panel as well.

In order to assess the relative contributions of temperature and humidity fluctuations to refractive index variability in terms of C_n^2, the vertical distributions of the individual terms in Eq. (11) have been considered. Figure 5 shows these distributions for simulations LES10 (left) and LES10EMF (right). All terms shown have been evaluated along the *x* direction. Corresponding profiles of $C_n^2\big|_y$ and $C_n^2\big|_{zp}$, and individual terms contributing to these quantities (not shown here) look very similar to the distributions illustrated in Fig. 5.

For both simulations LES10 and LES10EMF, the C_T^2 term dominates the C_n^2 budget in the lower portion of the CBL. The relatively weak surface latent heat flux in simulation LES10 results in both C_q^2 and C_{Tq} terms being relatively small near the surface compared to their values in simulation LES10EMF. The C_q^2 term from LES10EMF exhibits a near-surface maximum as a result of the enhanced surface latent heat flux. Even with this maximum and the increase in near-surface values of the C_{Tq} term in simulation LES10EMF, the C_T^2 term remains dominant.

The difference in the height at which the C_{Tq} term becomes negative in simulations LES10 and LES10EMF is worth noting. The prescription of an enhanced latent heat flux in simulation LES10EMF causes this transition of C_{Tq} to negative values to occur at greater heights than in simulation LES10. This difference can be important because total C_n^2 can be significantly reduced as the magnitude of the negative C_{Tq} term values becomes larger

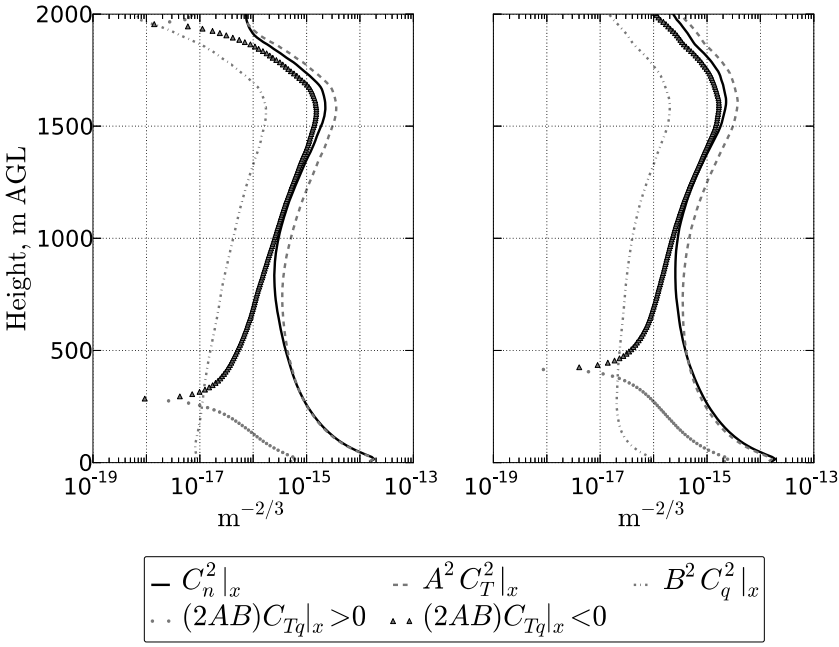

Fig. 5. Vertical distribution of $C_n^2\big|_x$ and individual contributing terms in Eq. (11) for simulations LES10 (left) and LES10EMF (right). Structure function values correspond to a separation distance of 60 m and a wavelength of 0.55 μm. The triangles represent negative values of the second term on the right-hand side of Eq. (11).

above this transition height as a result of the entrainment process. The influence of the negative C_{Tq} term on total C_n^2 is clearly seen in both panels of Fig. 5.

4. CONCLUSIONS

Approaches toward direct evaluation of refractive index structure functions and structure-function parameters from LES output for atmospheric CBL have been investigated. Feasibility of the direct retrieval of the refractive-index structure-function parameters from LES output for a moderately sheared CBL has been demonstrated.

Two direct evaluation methods have been compared. The first method involves calculating the refractive index at each point in the simulation domain with subsequent calculation of the refractive-index structure function. The second method is based on a parameterized linear relationship between the refractive index structure function and temperature, humidity, and temperature-humidity structure functions. The latter functions have been

directly evaluated from the LES temperature and humidity fields. Either method provides structure functions that correspond to different spatial separations expressed as integer multiples of the LES numerical grid spacing.

Structure functions evaluated through both methods have been analyzed for two CBL simulation outputs with 10-m grid spacing. One simulation featured an enhanced surface latent heat flux relative to the other. Both evaluation methods yield refractive-index structure function values that follow the 2/3-law throughout an extended range of separations in the well-mixed portion of the CBL. The lower limit of the 2/3-law behavior is dependent upon the LES spatial resolution and appears to be about four times the LES grid spacing (which was spatially uniform in the conducted LES).

For each evaluation method, vertical profiles of C_n^2 computed for separations along the x, y, and z directions have been shown to collapse together over a significant portion of the CBL. Near-surface divergence of C_n^2 values along the horizontal directions was noted and attributed to the influence of surface wind shear on the turbulent fluctuations of temperature and humidity. The behavior of C_n^2 near the surface was shown to agree favorably with MOST predictions.

Spatial variability in the temperature field was found to be the dominant contributor to visible-radiation C_n^2 values near the surface for both simulations considered. Aloft, the joint temperature-humidity structure function parameter reaches relatively large-magnitude negative values as a result of entrainment. This effect acts to reduce the total C_n^2 in the upper portion of the CBL.

Acknowledgement. Authors gratefully acknowledge discussions with Phillip Chilson, Richard Doviak, and Robert Palmer. Presented research was supported, in part, by the National Science Foundation, USA, through the grant ATM-1016153.

References

Andreas, E.L. (1988), Estimating C_n^2 over snow and sea ice from meteorological data, *J. Opt. Soc. Am. A* **5**, 4, 481-495, DOI: 10.1364/JOSAA.5.000481.

Benjamin, S.G., K.J. Brundage, and L.L. Morone (1994), *Implementation of the Rapid Update Cycle. Part I: Analysis/Model Description*, NOAA/NWS Technical Procedures Bull., 16 pp.

Burk, S.D. (1980), Refractive index structure parameters: Time-dependent calculations using a numerical boundary-layer model, *J. Appl. Meteor.* **19**, 5, 562-576, DOI: 10.1175/1520-0450(1980)019<0562:RISPTD>2.0.CO;2.

Cheinet, S., and P. Cumin (2011), Local structure parameters of temperature and humidity in the entrainment-drying convective boundary layer: A large-eddy simulation analysis, *J. Appl. Meteor. Climatol.* **50**, 2, 472-481, DOI: 10.1175/2010JAMC2426.1.

Cheinet, S., and A.P. Siebesma (2009), Variability of local structure parameters in the convective boundary layer, *J. Atmos. Sci.* **66**, 4, 1002-1017, DOI: 10.1175/2008JAS2790.1.

Cook, D.R., and M.S. Pekour (2008), Eddy correlation flux measurement systems handbook, Tech. Rep. DOE/SC-ARM/TR-05, 15 pp.

Corrsin, S. (1951), On the spectrum of isotropic temperature fluctuations in an isotropic turbulence, *J. Appl. Phys.* **22**, 4, 469-473, DOI: 10.1063/1.1699986.

Deardorff, J.W. (1980), Stratocumulus-capped mixed layers derived from a three-dimensional model, *Bound.-Layer Meteorol.* **18**, 4, 495-527, DOI: 10.1007/BF00119502.

Essenwanger, O., and E.R. Reiter (1969), Power spectrum, structure function, vertical wind shear, and turbulence in troposphere and stratosphere, *Arch. Met. Geoph. Biokl*. A, **18**, 17-24, DOI: 10.1007/BF02247861.

Fedorovich, E., R. Conzemius, and D. Mironov (2004a), Convective entrainment into a shear-free, linearly stratified atmosphere: Bulk models reevaluated through large eddy simulations, *J. Atmos. Sci.* **61**, 3, 281-295, DOI: 10.1175/1520-0469(2004)061<0281:CEIASL>2.0.CO;2.

Fedorovich, E., R. Conzemius, I. Esau, F. Katopodes Chow, D. Lewellen, C.-H. Moeng, D. Pino, P. Sullivan, and J. Vilà-Guerau de Arellano (2004b), Entrainment into sheared convective boundary layers as predicted by different large eddy simulation codes. **In:** *16th Symp. on Boundary Layers and Turbulence*, P. 4.7, Amer. Meteor. Soc., Portland, ME.

Frederickson, P.A., K.L. Davidson, C.R. Zeisse, and C.S. Bendall (2000), Estimating the refractive index structure parameter (C_n^2) over the ocean using bulk methods, *J. Appl. Meteor.* **39**, 1770-1783, DOI: 10.1175/1520-0450-39.10.1770.

Gibbs, J.A., E. Fedorovich, and A.M.J. van Eijk, (2011), Evaluating Weather Research and Forecasting (WRF) model predictions of turbulent flow parameters in a dry convective boundary layer, *J. Appl. Meteor. Climatol.* **50**, 12, 2429-2444, DOI: 10.1175/2011JAMC2661.1.

Kaimal, J.C., J.C. Wyngaard, D.A. Haugen, O.R. Cotè, Y. Izumi, S.J. Caughey, and C.J. Readings (1976), Turbulence structure in the convective boundary layer, *J. Atmos. Sci.* **33**, 2152-2169, DOI: 10.1175/1520-0469(1976)033<2152:TSITCB>2.0.CO;2.

Kohsiek, W. (1988), Observation of the structure parameters C^2_T, C_{TQ}, and C^2_Q in the mixed layer over land, *Appl. Opt.* **27**, 11, 2236-2240, DOI: 10.1364/AO.27.002236.

McBean, G.A., and J.A. Elliott (1981), Pressure and humidity effects on optical refractive-index fluctuations, *Bound.-Layer Meteorol.* **20**, 1, 101-109, DOI: 10.1007/BF00119926.

Obukhov, A.M. (1949), The structure of the temperature field in a turbulent flow, *Izv. Akad. Nauk SSSR, Geogr. Geogiz.* **13**, 1, 58-69 (in Russian).

Peltier, L.J., and J.C. Wyngaard (1995), Structure-function parameters in the convective boundary layer from large-eddy simulation, *J. Atmos. Sci.* **52**, 21, 3641-3660, DOI: 10.1175/1520-0469(1995)052<3641:SPITCB>2.0.CO;2.

Tatarskii, V.I. (1961), *Wave Propagation in a Turbulent Medium*, McGraw-Hill, New York, 285 pp.

van den Kroonenberg, A.C., S. Martin, F. Beyrich, and J. Bange (2012), Spatially-averaged temperature structure parameter over a heterogeneous surface measured by an unmanned aerial vehicle, *Bound.-Layer Meteorol.* **142**, 1, 55-77, DOI: 10.1007/s10546-011-9662-9.

Wyngaard, J.C. (2010), *Turbulence in the Atmosphere*, Cambridge University Press, New York, 393 pp.

Wyngaard, J.C., and O.R. Coté (1971), The budgets of turbulent kinetic energy and temperature variance in the atmospheric surface layer, *J. Atmos. Sci.* **28**, 2, 190-201, DOI: 10.1175/1520-0469(1971)028<0190:TBOTKE>2.0.CO;2.

Wyngaard, J.C., and M.A. LeMone (1980), Behavior of the refractive index structure parameter in the entraining convective boundary layer, *J. Atmos. Sci.* **37**, 7, 1573-1585, DOI: 10.1175/1520-0469(1980)037<1573:BOTRIS>2.0.CO;2.

Wyngaard, J.C., W.T. Pennell, D.H. Lenschow, and M.A. LeMone (1978), The temperature-humidity covariance budget in the convective boundary layer, *J. Atmos. Sci*. **35**, 1, 47-58, DOI: 10.1175/1520-0469(1978)035<0047:TTHCBI>2.0.CO;2.

Wyngaard, J.C., Y. Izumi, and S.A. Collins, Jr. (1971), Behavior of the refractive-index-structure parameter near the ground, *J. Opt. Soc. Am.* **61**, 12, 1646-1650, DOI: 10.1364/JOSA.61.001646.

Received 16 June 2012
Accepted 20 July 2012